Dual-Channel Airborne SAR Imaging of Ground Moving Targets on Perturbed Platform

Dau-Ming Wu and Jean-Fu Kiang, *Life Senior Member, IEEE*

***Abstract*— A dual-channel airborne synthetic aperture radar (SAR) imaging approach is proposed to acquire well-focused images of ground moving targets (GMTs) after compensating for the platform trajectory deviation (PTD). The phase error attributed to either PTD or target motion is given by a polynomial of slow time. The SAR image before motion compensation is segmented into multiple subimages, and a compressive-sensing (CS) technique is applied on each subimage to estimate the polynomial coefficients featuring PTD. A range-frequency reversal transform (RFRT) and fractional Fourier transform (FrFT) are combined to estimate the motion parameters and position of each moving target. The proposed approach is verified with real data and simulated data, respectively, and the moving targets in the acquired image are well recognized.**

***Index Terms*— Compressive sensing (CS), dual-channel, focusing, fractional Fourier transform (FrFT), ground moving target (GMT), platform trajectory deviation (PTD), range-frequency reversal transform (RFRT), synthetic aperture radar (SAR).**

I. Introduction

Airborne synthetic aperture radar (SAR) techniques have been widely used for imaging of ground moving targets (GMTs) in battlefield surveillance [1] and urban traffic monitor [2]. The image of a moving target is usually blurred beyond recognition due to its motion [3]. The phase error induced by target motion impedes conventional range-Doppler algorithms from focusing the images in the azimuth direction [4]. Several methods have been proposed to compensate for such effects. In [5], a second-order keystone transform (SOKT) was proposed to compensate for high-order range-walk error. Autofocusing of moving targets can be formulated as an optimization problem, which is then solved by using techniques such as compressive sensing (CS) [3], alternating direction method of multiplier (ADMM) and robust principal component analysis (RPCA) [6], [7].

In [3], a CS-based single-channel SAR imaging approach was proposed to focus smeared GMT image in a target region. The smeared target image was extracted first, on which an inverse cross-range compression process was applied. The phase error induced by target motion was represented as a polynomial, and the coefficients were estimated with a modified orthogonal matching pursuit (MOMP) and a Pearson correlation coefficients (PCCs) approach. A compensation filter was then designed to focus the GMT image.

In [8], application of machine learning methods, including convolutional neural network (CNN), to acquire high-quality SAR/ISAR images under sparse aperture conditions were briefly reviewed and compared with conventional CS-based imaging methods. In [9], a structured low-rank and sparse (SLR + S) approach was proposed to restore sparse sampling patterns such as random missing sampling (RMS) or gap missing sampling (GMS), followed by a fast ADMM to acquire ISAR images.

The pulse repetition frequency (PRF) of a wide-swath SAR surveillance system must be kept sufficiently low to avoid range ambiguity, thus causing azimuth ambiguity and manifesting ghost targets. In [10], a locating processing weighted group lasso (LP-W-GL) approach was proposed for SAR imaging on maritime targets. The weights on the target samples were increased to suppress clutters and mitigate ghost targets in the acquired SAR images.

A target moving too fast may induce Doppler ambiguity. In [11], a modified Keystone transform was proposed to resolve such an issue. In [12], the Doppler ambiguity problem was solved by estimating the first-order phase error with a 2-D scaled Fourier transform (SCFT) and estimating the second-order phase error with an improved range frequency cross correlation function (IRFCCF). However, the residual background signals may compromise the estimation. In [13], the cross-track velocity of a moving target was estimated from the slope of the range walk with Hough transform, and the range cell migration was corrected with a SOKT. An adaptive polynomial Fourier transform was applied to estimate the high-order phase error associated with the along-track acceleration of the moving target.

SAR images of moving targets can be better focused if the background signals are removed before processing the target [14]. For targets moving at low speed or immersed in a wide or complicated background, their restored images tended to be affected by clutters and became difficult to recognize [15], With a single-channel SAR approach, the Doppler shift induced by a moving target mingles with that of radar motion, creating ambiguity in the estimated azimuth position of the target [16], [17]. Multichannel approaches, such as space-time adaptive processing [18] and displaced phase center antenna (DPCA) [19], were proposed to correct the azimuth position of the target.

Manuscript received 25 December 2022; revised 21 February 2023; accepted 27 March 2023. Date of publication 7 April 2023; date of current version 20 April 2023. *(Corresponding author: Jean-Fu Kiang.)*

The authors are with the Graduate Institute of Communication Engineering, National Taiwan University, Taipei 10617, Taiwan (e-mail: jfkiang@ntu.edu.tw).

Digital Object Identifier 10.1109/TGRS.2023.3265408

In practice, the radar platform may not always maintain a straight flight path or constant velocity due to atmospheric perturbations, resulting in range error and blurred images [20]. Modern inertial navigation system (INS) and global positioning system (GPS) [21] can compensate for flight path deviation or fluctuating velocity to some extent. The residual phase error [21] is called platform trajectory deviation (PTD) error in this work.

Various autofocusing approaches have been proposed to mitigate the PTD error, including phase gradient algorithm (PGA) [22], [23], map drift [24], [25], [26], optimization method [27], [28], maximum contrast [29], and minimum entropy [30].

In [22], a PGA in conjunction with linear unbiased minimum variance (LUMV) was proposed to estimate the phase gradient versus slow time, and the phase error across the full aperture was obtained by integrating the phase gradient. However, this method worked only when strong scatterers were present in the target area [29], [31].

In [25], a 2-D spatial-variant map-drift autofocusing technique was proposed to compensate for both range and azimuth-dependent phase errors. In [26], full-aperture signals were alloted to multiple subapertures, and a map-drift autofocusing approach was applied to estimate the local phase error and platform acceleration. The platform trajectory across the full aperture was derived by integrating the estimated acceleration on all the subapertures.

In [27], improved Tikhonov regularization (ITR) and CS techniques were proposed to find the optimal solutions for autofocusing SAR images, under the conditions that the received signals were sparse, embedding random phase error or at low SNR. In [28], full-aperture signals were allotted to multiple subapertures, with the phase error on each subaperture estimated by solving an optimization problem.

Most SAR imaging methods on moving targets presumed stationary background, and the background signals were usually removed before focusing on the moving targets [32]. Some residual background signals will blur the image of moving targets, and the presence of platform perturbation will blur the image of both background and moving targets [33]. The effects of platform perturbation and the target motion are intertwined in the received signals and cannot be separated directly. The range error associated with a moving target is attributed to both motions, while that associated with the stationary background is attributed to platform perturbation. In this work, separate autofocusing approaches are applied to restore the images of moving targets and backgrounds, respectively. A SAR image acquired with a conventional range-Doppler algorithm is first segmented into several subimages, with only a few of them affected by moving targets. The phase error caused by PTD is estimated and compensated by using the subimages less affected by the moving targets. An entropy-based target detection method is then applied to narrow down the subimages containing moving targets. The image of each moving target is focused via iterative forward and inverse processes, and its motion parameters are estimated with an RFRT-FrFT method. Finally, the motion parameters derived from dual channels are used to estimate the position of each moving target.

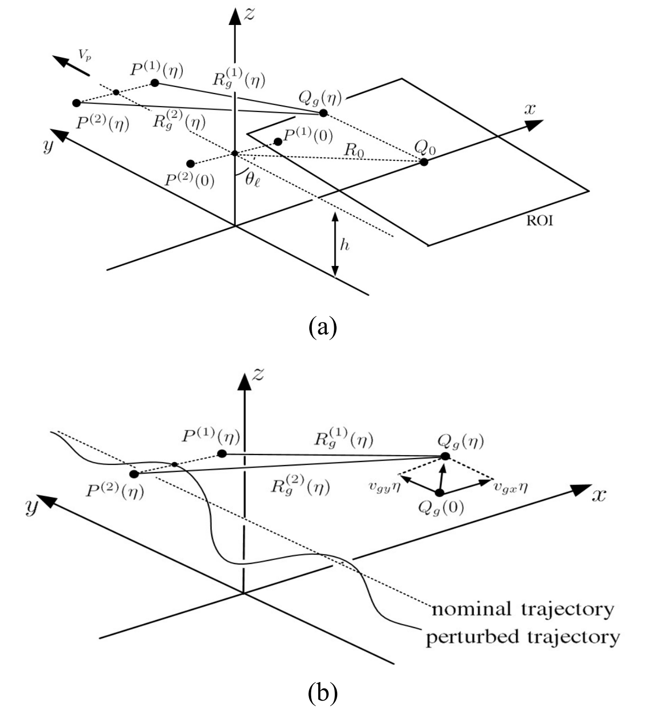

Fig. 1. Schematic of dual-channel airborne SAR imaging (a) on stationary target with straight platform trajectory and (b) on GMT with PTD.

The rest of this work is organized as follows. The range model and proposed approach are presented in Section II, a CS technique is proposed to compensate for the phase error due to platform trajectory deviation in Section III, an imaging approach on moving targets is proposed in Section IV, target recognition, verification on real data and highlights are presented in Section V, and some conclusions are drawn in Section VI.

II. Range Model and Proposed Approach

Fig. 1 shows the schematic of dual-channel airborne SAR imaging on a GMT, under the influence of PTD. The platform without perturbation is supposed to move at a constant speed V_p and at height h above ground. Two radars are installed on the platform, separated by d across the track, operating at look angle θ_ℓ. The region of interest (ROI) is centered at a reference point $Q_0 = (x_0, 0, 0)$, the gth moving target is located at $Q_g(\eta)$ at slow time η, with $Q_g(0) = (x_0+x_{g0}, y_{g0}, 0)$. Radar s ($s = 1, 2$) is located at $P^{(s)}(\eta)$, with $P^{(1)}(0) = (d/2, 0, h)$ and $P^{(2)}(0) = (-d/2, 0, h)$. The range between radar s and the gth moving target is $R_g^{(s)}(\eta) = |\overline{Q_g(\eta)P^{(s)}(\eta)}|$. The proposed approach is applied to acquire the images of moving targets in the ROI, under residual PTD.

In the absence of PTD, the range between radar s and a stationary point target at $(x_0 + x_n, y_n, 0)$ is given by the following equation:

$$R_n^{(s)}(\eta) = \sqrt{(x_0 \mp d/2 + x_n)^2 + (y_n - V_p\eta)^2 + h^2}$$
$$\simeq R_{0n}^{(s)} - \frac{V_p y_n}{R_0^{(s)}}\eta + \frac{V_p^2}{2R_0^{(s)}}\eta^2, \quad s = 1, 2 \qquad (1)$$

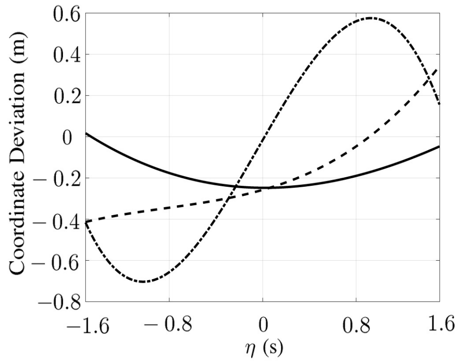

Fig. 2. Example of PTD [34], ———: in x direction, $- \cdot -$ in y direction, $- - -$: in z direction.

where $R_{0n}^{(s)} = ((x_0 \mp d/2 + x_n)^2 + y_n^2 + h^2)^{1/2}$, with $s = 1, 2$, and $R_0^{(s)} = ((x_0 \mp d/2)^2 + h^2)^{1/2}$ is the closest range between radar s and the reference point.

Assume the gth target moves at a velocity of $\hat{x}v_{gx} + \hat{y}v_{gy}$, and its backscattered signal is contributed by N_g scatterers, with the nth scatterer located at $Q_{gn}(\eta) = (x_0 + x_{g0} + x_{gn} + v_{gx}\eta, y_{g0} + y_{gn} + v_{gy}\eta, 0)$. The range between the nth scatterer and radar s is given by the following equation:

$$\begin{aligned} R_{gn}^{(s)}(\eta) &= \left|\overline{Q_{gn}(\eta)P^{(s)}(\eta)}\right| \\ &= \Big\{(x_0 \mp d/2 + x_{g0} + x_{gn} + v_{gx}\eta)^2 \\ &\qquad + [y_{g0} + y_{gn} + (v_{gy} - V_p)\eta]^2 + h^2\Big\}^{1/2} \\ &\qquad\qquad s = 1, 2 \end{aligned}$$

The difference between $R_{gn}^{(s)}(\eta)$ and $R_{0n}^{(s)}$ is referred to as the GMT range error, which can be approximated by a second-order polynomial of η as follows [3]:

$$\Delta R_g^{(s)}(\eta) = R_{gn}^{(s)}(\eta) - R_{0n}^{(s)} \simeq \gamma_{g1}^{(s)}\eta + \gamma_{g2}^{(s)}\eta^2 \tag{2}$$

where the first-order term and the second-order term induce an azimuth position shift and blurring, respectively, of the moving target in the acquired image, with the coefficients given by the following equation:

$$\gamma_{g1}^{(s)} = \frac{v_{gx}(x_0 \mp d/2 + x_{g0}) + (v_{gy} - V_p)y_{g0}}{R_0^{(s)}} \tag{3}$$

$$\begin{aligned} \gamma_{g2}^{(s)} &= \frac{v_{gx}^2 + (v_{gy} - V_p)^2}{2R_0^{(s)}} \\ &\quad - \frac{\left[v_{gx}(x_0 \mp d/2 + x_{g0}) + (v_{gy} - V_p)y_{g0}\right]^2}{2\left(R_0^{(s)}\right)^3}. \end{aligned} \tag{4}$$

We use the data shown in Fig. 2 [34] to simulate the residual PTD after correction with INS or GPS technique. Similarly, the range between a stationary background scatterer at $(x_0 + x_n, y_n)$ and radar s is given by the following equation [20]:

$$R_{bn}^{(s)}(\eta) = R_n^{(s)}(\eta) + \Delta R_p^{(s)}(\eta) \tag{5}$$

where $\Delta R_p^{(s)}(\eta)$ is approximated with a third-order polynomial of η as follows [35]:

$$\Delta R_p^{(s)}(\eta) \simeq \beta_1^{(s)}\eta + \beta_2^{(s)}\eta^2 + \beta_3^{(s)}\eta^3. \tag{6}$$

TABLE I

DEFAULT PARAMETERS USED IN SIMULATIONS

parameter	symbol	proposed	ref.
carrier frequency	f_c	10 GHz	[25]
range bandwidth	B_r	2,000 MHz	[24]
range sampling rate	F_r	2,400 MHz	[28]
pulse duration	T_r	20 μs	[26]
range chirp rate	K_r	100 THz/s	[25]
pulse repetition frequency	F_a	1,000 Hz	[25]
coherent time	T_a	2.05 s	
look angle	θ_ℓ	45°	[26]
elevation beamwidth	θ_{el}	40°	[26]
azimuth beamwidth	θ_{az}	10°	[26]
squint angle	θ_q	0°	[37]
platform height	h	5 km	[24]
platform velocity	V_p	120 m/s	[24]
spacing between radars	d	20 m	
aperture length	L_a	246 m	
closest slant range	R_0	7.07 km	

By superposing the range errors attributed to both target motion and platform perturbation, the range between the gth moving target can be approximated as follows:

$$R_{gn}^{(s)}(\eta) = R_{0n}^{(s)} + \Delta R_g^{(s)}(\eta) + \Delta R_p^{(s)}(\eta). \tag{7}$$

The transmitted signal is a linear frequency modulation (LFM) pulse

$$s_0(\tau) = \text{rect}\,(\tau/T_r)\, e^{j2\pi f_c \tau} e^{j\pi K_r \tau^2}$$

where f_c is the carrier frequency, K_r is the chirp rate, T_r is the pulsewidth, and

$$\text{rect}(t) = \begin{cases} 1, & |t| \le 1/2 \\ 0, & \text{otherwise} \end{cases}$$

is a window function.

The backscattered signal after demodulation is given by the following equation:

$$\begin{aligned} s_1^{(s)}(\tau, \eta) &= \sum_{n=1}^{N} A_n^{(s)} \text{rect}\left(\frac{\tau - \tau_n^{(s)}}{T_r}\right) \\ &\quad \times e^{-j4\pi f_c R_n^{(s)}(\eta)/c} e^{j\pi K_r \left(\tau - \tau_n^{(s)}\right)^2} \end{aligned} \tag{8}$$

where N is the number of scatterers, $A_n^{(s)}$ is the backscattering coefficient of the nth scatterer, and $\tau_n^{(s)} = 2R_n^{(s)}(\eta)/c$. The range models in (5) and (7) are used for stationary background and moving target, respectively.

In practice, the image on an ROI can be acquired by extracting the received signals in specific fast-time intervals and Doppler frequency bands, respectively. Fig. 3(a) shows an X-band SAR image of a region in Wachtberg, Germany [36], to simulate the background image. By comparing the background intensity with that of metal objects in the image, the backscattering coefficients are calibrated over the interval of 0.25–0.45, with 1.0 for metal objects. Fig. 3(c) shows a 3-D model of an M1A2 Abrams tank to simulate a GMT, which is approximated as a perfect electric conductor and its backscattered signals are computed with physical optics (PO) theory.

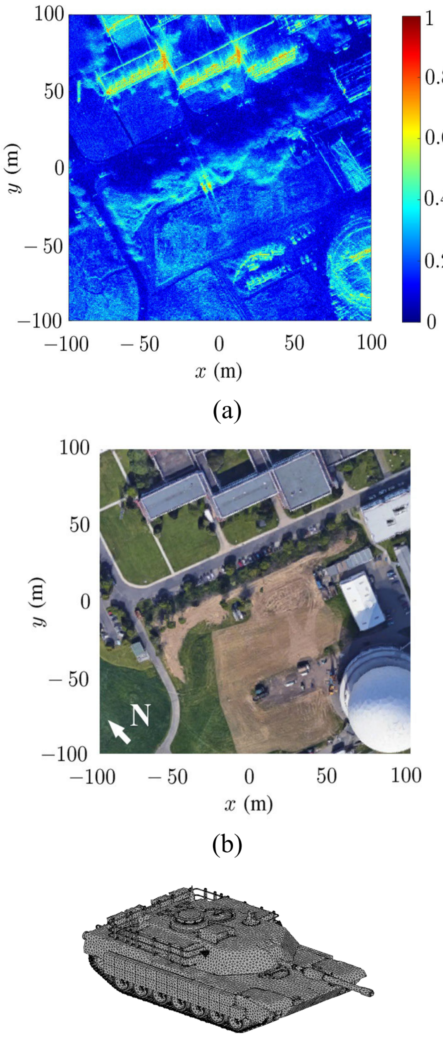

Fig. 3. (a) X-band SAR image centered at (50°37′2″N, 7°7′42.2″ E), Wachtberg, Germany [36], (b) same region on Google Earth, and (c) model of M1A2 Abrams.

TABLE II

MOTION PARAMETERS OF GMTS

GMT	x_{g0}(m)	y_{g0}(m)	v_{gx}(m/s)	v_{gy}(m/s)
$g = 1$	10	-20	3	6
$g = 2$	-42	32	-2	12

Table I lists the default parameters used in the simulations. Based on these parameters, slight uncertainty of scatterer height or scatterer position by about 5 cm may shift the phase of backscattered signal over 2π. Hence, the phase in each pixel is picked randomly from $[-\pi, \pi)$ in this work. Two M1A2 Abrams tanks are simulated as moving targets, with their initial position and velocity components listed in Table II.

Fig. 4 shows the flowchart of the proposed iterative two-stage SAR imaging approach, which is capable of focusing the images of the background and the moving targets separately. Fig. 5 shows the breakdown flow-charts of RDA, IRDA, and IRDA$_g$, respectively, and Fig. 6 shows the breakdown flow-charts of the PTD autofocusing and GMT autofocusing, respectively. Compositional processes in these flow-charts can be found in [18] and [40]. Different surveillance modes for airborne SAR applications were discussed in [38], and some commonly used autofocusing approaches were presented in [39] and [40].

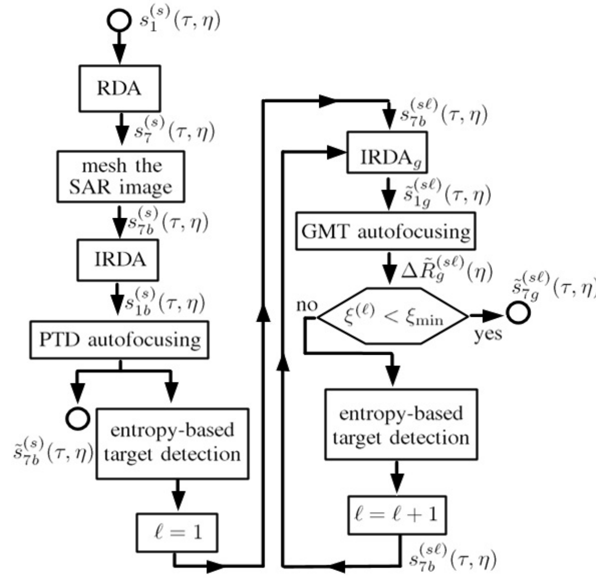

Fig. 4. Flowchart of iterative two-stage SAR imaging approach.

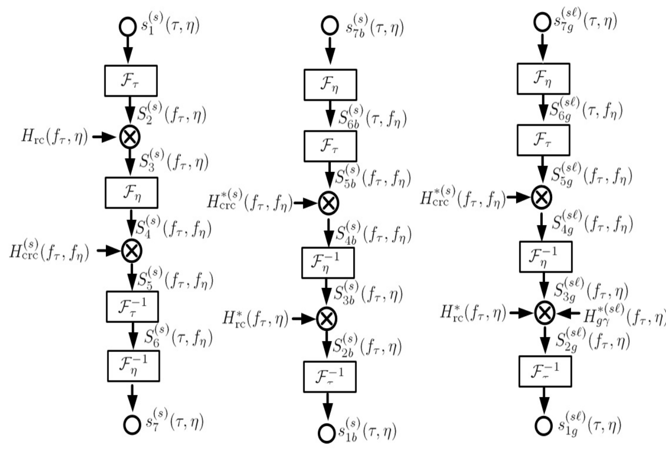

Fig. 5. Flow-charts of (a) RDA, (b) IRDA, and (c) IRDA$_g$ in Fig. 4.

III. COMPENSATION OF PHASE ERROR DUE TO PTD

Fig. 7(a) shows the original SAR image without any compensation. The spatial resolutions are $\Delta x = 0.21$ m and $\Delta y = 0.2$ m. The image of the stationary background is smeared by the PTD phase error, while the areas around the GMTs, as enclosed by white rectangles, are smeared by both GMT and PTD phase errors. The GMT phase error tends to spread over a wider area than its residing pixels in the acquired image, and the outward infiltration of GMT phase error is exacerbated by the fact that the backscattered signals from GMTs are much stronger than those from the surrounding background.

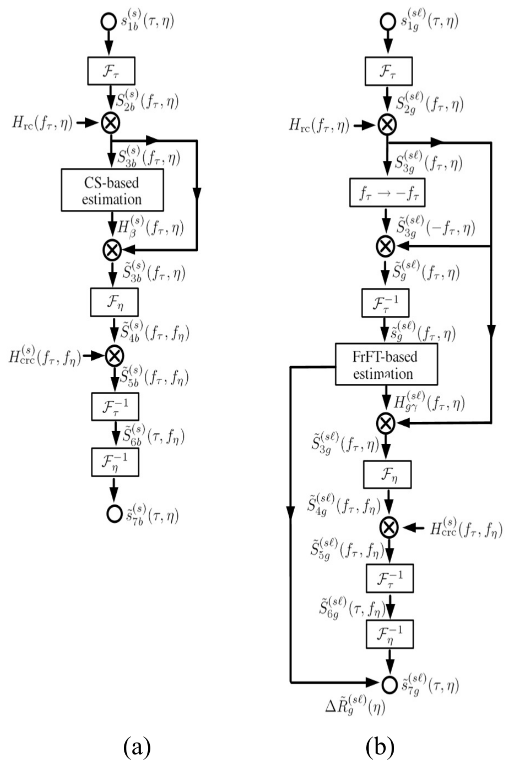

Fig. 6. Flow-charts of (a) PTD autofocusing and (b) GMT autofocusing in Fig. 4.

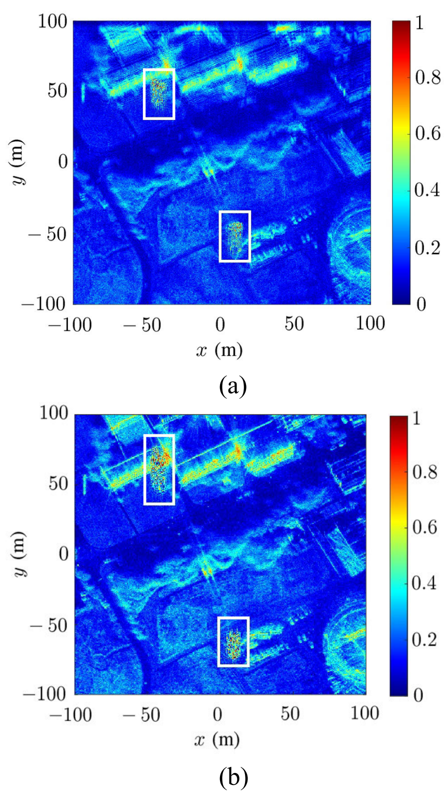

Fig. 7. Acquired SAR image (a) without compensation and (b) with PTD compensation. Areas affected by GMT are enclosed with a white rectangle.

The number of pixels smeared by GMT phase error takes a small percentage of pixels. Thus, the pixels unaffected by the GMT phase error will be used to estimate the PTD phase error. First, we divide the SAR image in Fig. 7(a) into 64 subimages of equal size (about 25 × 25 m), and apply the inverse RDA in Fig. 5(a) on each subimage to restore the corresponding backscattered signals as in (8). These subimages are expected to bear the PTD phase error specified in (6).

The restored backscattered signals after applying the inverse RDA to a subimage is given by the following equation:

$$s_{1b}^{(s)}(\tau,\eta) = \sum_{n=1}^{N_b} A_{bn}^{(s)} \text{rect}\left(\frac{\tau-\tau_{bn}^{(s)}}{T_r}\right) \times e^{-j4\pi f_c R_{bn}^{(s)}(\eta)/c} e^{j\pi K_r\left(\tau-\tau_{bn}^{(s)}\right)^2}$$

where N_b is the number of background scatterers in the subimage, $A_{bn}^{(s)}$ and $\tau_{bn}^{(s)}$ are the backscattering coefficient and time delay, respectively, from the nth scatterer, with

$$\tau_{bn}^{(s)} = 2\left[R_n^{(s)}(\eta) + \Delta R_p^{(s)}(\eta)\right]/c.$$

Next, take the range Fourier transform of $s_{1b}^{(s)}(\tau,\eta)$ to have

$$S_{2b}^{(s)}(f_\tau,\eta) = \mathcal{F}_\tau\left\{s_{1b}^{(s)}(\tau,\eta)\right\} = \sum_{n=1}^{N_b} A_{bn}^{(s)} \text{rect}\left(f_\tau/B_r\right) \times e^{-j\pi f_\tau^2/K_r} e^{-j4\pi(f_c+f_\tau)\left[R_n^{(s)}(\eta)+\Delta R_p^{(s)}(\eta)\right]/c}$$

which is multiplied with a range compression filter $H_{\text{rc}}(f_\tau) = e^{j\pi f_\tau^2/K_r}$ to obtain

$$S_{3b}^{(s)}(f_\tau,\eta) = S_{2b}^{(s)}(f_\tau,\eta)H_{\text{rc}}(f_\tau) = \sum_{n=1}^{N_b} A_{bn}^{(s)} \text{rect}\left(f_\tau/B_r\right) \times e^{-j4\pi(f_c+f_\tau)\left[R_n^{(s)}(\eta)+\Delta R_p^{(s)}(\eta)\right]/c}. \quad (9)$$

A. Estimation of PTD Range Error

Next, a CS technique is applied to each subimage to estimate the coefficients $\beta_1^{(s)}$, $\beta_2^{(s)}$ and $\beta_3^{(s)}$ of PTD range error $\Delta R_p^{(s)}(\eta)$ in (6). The values of $S_{3b}^{(s)}(0,\eta_m)$'s of the subimage are first vectorized as $\bar{S}_{3b}^{(s)} = [S_{3b}^{(s)}[1], S_{3b}^{(s)}[2], \ldots, S_{3b}^{(s)}[N_a]]^t$, where $\eta_m = (-N_a/2+m-1)/F_a$, $S_{3b}^{(s)}[m] = S_{3b}^{(s)}(0,\eta_m)$ as in (9), and $R_n^{(s)}[m] = R_n^{(s)}(\eta_m)$ as in (1). Note that strong reference scatterers are not required as with the PGA [29], [31].

Then, compute atoms of a dictionary as follows [41]:

$$\bar{\psi}^{(s)}(\bar{\beta}) = \begin{bmatrix} \sum_{n=1}^{N_b} e^{-j4\pi f_c R_n^{(s)}[1]/c} \\ \sum_{n=1}^{N_b} e^{-j4\pi f_c R_n^{(s)}[2]/c} \\ \vdots \\ \sum_{n=1}^{N_b} e^{-j4\pi f_c R_n^{(s)}[N_a]/c} \end{bmatrix} \circ \begin{bmatrix} e^{-j4\pi f_c\left(\beta_1^{(s)}\eta_1+\beta_2^{(s)}\eta_1^2+\beta_3^{(s)}\eta_1^3\right)/c} \\ e^{-j4\pi f_c\left(\beta_1^{(s)}\eta_2+\beta_2^{(s)}\eta_2^2+\beta_3^{(s)}\eta_2^3\right)/c} \\ \vdots \\ e^{-j4\pi f_c\left(\beta_1^{(s)}\eta_{N_a}+\beta_2^{(s)}\eta_{N_a}^2+\beta_3^{(s)}\eta_{N_a}^3\right)/c} \end{bmatrix}$$

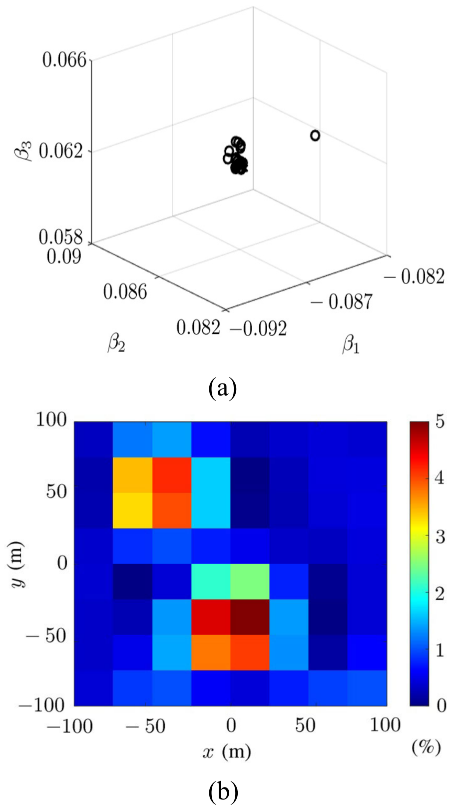

Fig. 8. Distribution of (a) estimated $\bar{\beta}$ and (b) estimation error ξ_β, over 64 subimages, $s = 1$.

where $\circ$ means direct product, the first vector represents the signal from the subimage area with uniform backscattering coefficient, and the second vector represents the PTD phase error. An atom is associated with a particular set of $\bar{\beta}^{(s)} = [\beta_1^{(s)}, \beta_2^{(s)}, \beta_3^{(s)}]^t$ on a 3-D grid, where $B_{1\min} \leq \beta_1^{(s)} \leq B_{1\max}$, $B_{2\min} \leq \beta_2^{(s)} \leq B_{2\max}$ and $B_{3\min} \leq \beta_3^{(s)} \leq B_{3\max}$. The grid spacing is $\Delta\beta_n = (B_{n\max} - B_{n\min})/U_n$, given U_n grid points, with $n = 1, 2, 3$. This dictionary $\bar{\bar{\Psi}}^{(s)}$ contains $U_1U_2U_3$ atoms.

With dictionary $\bar{\bar{\Psi}}^{(s)}$, $\bar{S}_{3b}^{(s)}$ is encoded as $\bar{S}_{3b}^{(s)} = \bar{\bar{\Psi}}^{(s)} \cdot \bar{x}_\beta^{(s)}$, where $\bar{x}_\beta^{(s)}$ is a coefficient vector of dimension $U_1U_2U_3$, which is determined by solving an optimization problem [42], [43]

$$\tilde{\bar{x}}_\beta^{(s)} = \arg\min_{\bar{x}_\beta^{(s)}} \left\|\bar{x}_\beta^{(s)}\right\|_1 \quad \text{s.t.} \left\|\bar{S}_{3b}^{(s)} - \bar{\bar{\Psi}}^{(s)} \cdot \bar{x}_\beta^{(s)}\right\|_2 \leq \varepsilon \tag{10}$$

where $\|\bar{x}_\beta^{(s)}\|_1$ is the 1-norm of $\bar{x}_\beta^{(s)}$, and ε is a tolerance. The optimization problem in (10) can be solved with the CVX tool [44]. The PTD range error in the subimage is given by the following equation:

$$\Delta\tilde{R}_p^{(s)}(\eta) = \tilde{\beta}_1^{(s)}\eta + \tilde{\beta}_2^{(s)}\eta^2 + \tilde{\beta}_3^{(s)}\eta^3.$$

Fig. 8(a) shows the estimated $\bar{\beta}$ vectors over 64 subimages segmented from Fig. 7(a). Most $\bar{\beta}$ vectors cluster around the true vector and only a few $\bar{\beta}$'s associated with subimages containing GMT signals deviate from the cluster center. The coefficients are estimated by taking the average over the clustering $\bar{\beta}$ vectors, and the results are listed in Table III.

TABLE III
COEFFICIENTS OF PTD RANGE ERROR

	β_1	β_2	β_3
true	-0.0877	0.0849	0.0621
estimated	-0.0874	0.0852	0.0614

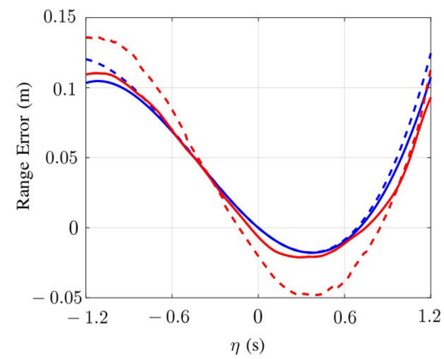

Fig. 9. Range errors, ——: true PTD range error, – – –: estimated with proposed approach, ——: estimated with PGA, – – –: estimated with PGA in the presence of GMTs.

Define an estimation error as $\xi_\beta = 100 \times |\tilde{\bar{\beta}} - \bar{\beta}|/|\bar{\beta}|$ (%), where $\tilde{\bar{\beta}}$ is the estimated vector of $\bar{\beta}$ on a subimage. Fig. 8(b) shows the estimation error over 64 subimages. The subimages with larger estimation error overlap with the blurred areas shown in Fig. 7(a).

Fig. 9 shows the PTD range error estimated with the proposed approach is very close to the true value. The range error estimated with the PGA [22] is slightly different from the true value in case there are no moving targets, but becomes larger if the effects of moving targets are included.

B. Compensation of Range Error

To compensate for the PTD range error embedded in the image of Fig. 7(a), first apply a compensation filter $H_\beta^{(s)}(f_\tau, \eta) = e^{j4\pi(f_c+f_\tau)\Delta\tilde{R}_p^{(s)}(\eta)/c}$ to $S_{3b}^{(s)}(f_\tau, \eta)$ as follows:

$$\begin{aligned}\tilde{S}_{3b}^{(s)}(f_\tau, \eta) &= S_{3b}^{(s)}(f_\tau, \eta)H_\beta^{(s)}(f_\tau, \eta)\\ &= \sum_{n=1}^{N_b} A_{bn}^{(s)} \mathrm{rect}\,(f_\tau/B_r)\, e^{-j4\pi(f_c+f_\tau)R_n^{(s)}(\eta)/c}\end{aligned}$$

which is Fourier transformed in azimuth to have

$$\begin{aligned}\tilde{S}_{4b}^{(s)}(f_\tau, f_\eta) &= \mathcal{F}_\eta\left\{\tilde{S}_{3b}^{(s)}(f_\tau, \eta)\right\} = \sum_{n=1}^{N_b} A_{bn}^{(s)} \mathrm{rect}\,(f_\tau/B_r)\\ &\quad \times e^{-j4\pi(f_c+f_\tau)R_{0n}^{(s)}/c} e^{j2\pi(f_c+f_\tau)y_{bn}^2/\left(cR_0^{(s)}\right)}\\ &\quad \times e^{-j2\pi f_\eta y_{bn}/V_p} e^{j\pi f_\eta^2 cR_0^{(s)}/\left[2(f_c+f_\tau)V_p^2\right]}\end{aligned}$$

and multiplied with a range compression filter $H_{\mathrm{crc}}^{(s)}(f_\tau, f_\eta) = e^{-j\pi f_\eta^2 cR_0^{(s)}/[2(f_c+f_\tau)V_p^2]}$ as follows:

$$\begin{aligned}\tilde{S}_{5b}^{(s)}(f_\tau, f_\eta) &= \tilde{S}_{4b}^{(s)}(f_\tau, f_\eta)H_{\mathrm{crc}}^{(s)}(f_\tau, f_\eta)\\ &= \sum_{n=1}^{N_b} A_{bn}^{(s)} \mathrm{rect}\,(f_\tau/B_r)\, e^{-j4\pi(f_c+f_\tau)R_{0n}^{(s)}/c}\\ &\quad \times e^{j2\pi(f_c+f_\tau)y_{bn}^2/\left(cR_0^{(s)}\right)} e^{-j2\pi f_\eta y_{bn}/V_p}.\end{aligned}$$

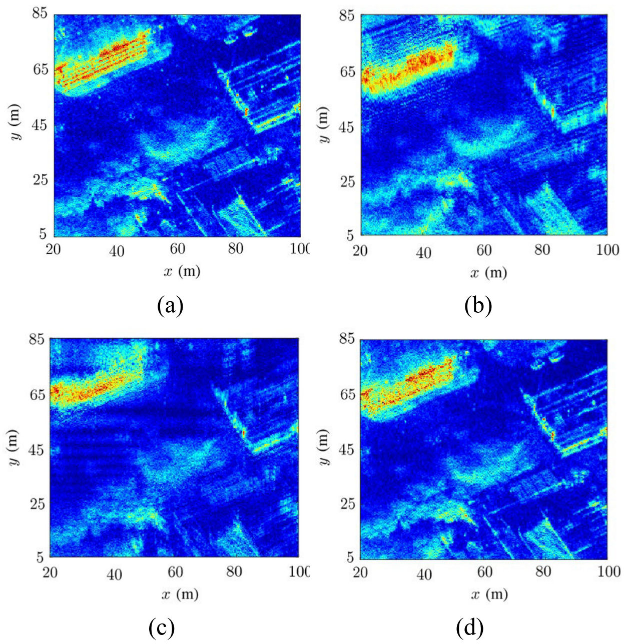

Fig. 10. Acquired images (a) without any phase error, (b) perturbed by PTD, (c) with PGA, and (d) with proposed CS-based PTD compensation.

By taking the inverse Fourier transform of $\tilde{S}_{5b}^{(s)}(f_\tau, f_\eta)$ in range, we have

$$\begin{aligned}\tilde{S}_{6b}^{(s)}(\tau, f_\eta) &= \mathcal{F}_\tau^{-1}\{\tilde{S}_{5b}^{(s)}(f_\tau, f_\eta)\}\\ &= \sum_{n=1}^{N_b} A_{bn}^{(s)} e^{-j4\pi f_c R_{0n}^{(s)}/c} e^{j2\pi f_c y_{bn}^2/\left(cR_0^{(s)}\right)}\\ &\quad \times e^{-j2\pi f_\eta y_{bn}/V_p}\\ &\quad \times B_r \operatorname{sinc}\left\{B_r\left[\tau - 2R_{0n}^{(s)}/c + y_{bn}^2/\left(cR_0^{(s)}\right)\right]\right\}\end{aligned}$$

which is inverse Fourier transformed in azimuth to have

$$\begin{aligned}\tilde{s}_{7b}^{(s)}(\tau, \eta) &= \mathcal{F}_\eta^{-1}\{\tilde{S}_{6b}^{(s)}(\tau, f_\eta)\}\\ &= \sum_{n=1}^{N_b} A_{bn}^{(s)} \operatorname{rect}(f_\tau/B_r) e^{-j4\pi f_c R_{0n}^{(s)}/c} e^{j2\pi f_c y_{bn}^2/\left(cR_0^{(s)}\right)}\\ &\quad \times B_r \operatorname{sinc}\left\{B_r\left[\tau - 2R_{0n}^{(s)}/c + y_{bn}^2/\left(cR_0^{(s)}\right)\right]\right\}\\ &\quad \times F_a \operatorname{sinc}\{F_a(\eta - y_{bn}/V_p)\}. \qquad (11)\end{aligned}$$

Fig. 7(b) shows the image after PTD compensation, most of the background image is well focused.

Fig. 10(a) and (b) show the acquired images with and without PTD range error, respectively. Fig. 10(c) and (d) show the images compensated with the PGA [22] and the proposed PTD compensation method, respectively. It is observed that the image compensated with PGA manifests artifacts of horizontal streaks, possibly affected by the presence of moving targets.

IV. Imaging of Moving Targets

A. Detection of GMTs With Entropy

A moving target can be detected in an image from the smeared area around it. In [32], an autofocusing approach was applied to each subimage segmented from a larger SAR image, and the output contrast was used to determine if moving targets were present in the subimage. The contrast was enhanced by multiplying the output with those from smaller subimages. In this work, a multiframe entropy-based detection method is applied to narrow down the image area containing moving targets.

Let the magnitude of SAR image in Fig. 7(b) after the ℓth iteration be $A^{(\ell)}(\tau, \eta) = |\tilde{s}_{7b}(\tau, \eta)|$, which is mapped to the xy plane as $A^{(\ell)}(x, y)$ for convenience of inspection. Divide the image into $K \times K$ subimages of equal area D_K. Compute the entropy of the wth subimage located in Z_{Kw} of the xy plane as follows [45]:

$$\mathcal{E}\{A_{Kw}^{(\ell)}\} = \frac{1}{D_K}\iint_{Z_{Kw}} A_{Kw}^{(\ell)}(x, y)\log_{10} A_{Kw}^{(\ell)}(x, y)dxdy$$

and a level-K entropy distribution over the whole image is given by the following equation:

$$E_K^{(\ell)}(x, y) = \mathcal{E}\{A_{Kw}^{(\ell)}\}, \quad (x, y) \in Z_{Kw}.$$

In the simulations, we choose $K = 8$, 16, 32, 64, and 128, corresponding to subimage sizes of 25 × 25 m, 12.5 × 12.5 m, 6.25 × 6.25 m, 3.125 × 3.125 m and 1.5625 × 1.5625 m, respectively. Fig. 11 shows the entropy distribution $E_K^{(1)}(x, y)$, with $K = 8$, 32, and 128, respectively. As the subimages get smaller, the whereabout of moving targets and finer background features become more obvious.

Next, compute an enhanced entropy distribution as follows:

$$E^{(\ell)}(x, y) = \prod_{K=8,16,32,64,128} E_K^{(\ell)}(x, y). \qquad (12)$$

Fig. 12(a) shows the enhanced entropy distribution after the first iteration. The blurred areas containing moving targets are smaller than their counterparts in Fig. 7(b).

Then, an IRDA process is applied on each blurred area to restore an equivalent received signal after demodulation associated with the gth moving target as follows:

$$s_{1g}^{(s\ell)}(\tau, \eta) = \sum_{n=1}^{N_g} A_{gn}^{(s)} \operatorname{rect}\left(\frac{\tau - \tau_{gn}^{(s)}}{T_r}\right) \times e^{-j4\pi f_c R_{gn}^{(s)}(\eta)/c} e^{j\pi K_r\left(\tau - \tau_{gn}^{(s)}\right)^2}$$

where N_g is the number of scatterers in the gth blurred area, $A_{gn}^{(s)}$ and τ_{gn} are the backscattering coefficient and time delay, respectively, of the nth scatterer, with $\tau_{gn}^{(s)} = 2[R_{0n}^{(s)} + \Delta R_g^{(s)}(\eta) + \Delta R_p^{(s)}(\eta)]/c$.

To compensate for the effect of target motion, first apply range compression to $s_{1g}^{(s\ell)}(\tau, \eta)$ by taking its range Fourier transform to have

$$S_{2g}^{(s)}(f_\tau, \eta) = \mathcal{F}_\tau\left\{s_{1g}^{(s\ell)}(\tau, \eta)\right\} \simeq \sum_{n=1}^{N_g} A_{gn}^{(s)} \operatorname{rect}(f_\tau/B_r) \times e^{-j\pi f_\tau^2/K_r} e^{-j4\pi(f_c+f_\tau)R_{gn}^{(s)}(\eta)/c}$$

and apply range-compression filter and PTD compensation filter to have

$$\begin{aligned}S_{3g}^{(s)}(f_\tau, \eta) &= S_{2g}^{(s)}(f_\tau, \eta) H_{\mathrm{rc}}(f_\tau) H_\beta^{(s)}(f_\tau, \eta)\\ &= \sum_{n=1}^{N_g} A_{gn}^{(s)} \operatorname{rect}(f_\tau/B_r)\\ &\quad \times e^{-j4\pi(f_c+f_\tau)\left[R_{0n}^{(s)} + \gamma_{g1}^{(s)}\eta + \gamma_{g2}^{(s)}\eta^2\right]/c} \qquad (13)\end{aligned}$$

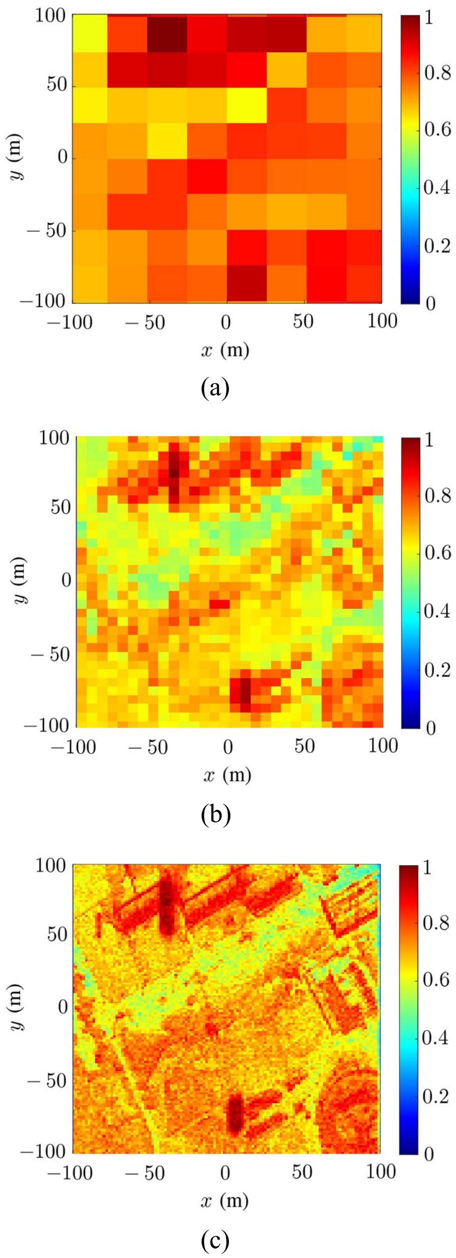

Fig. 11. Entropy distribution $E_K^{(1)}(x, y)$, (a) $K = 8$, (b) $K = 32$, and (c) $K = 128$.

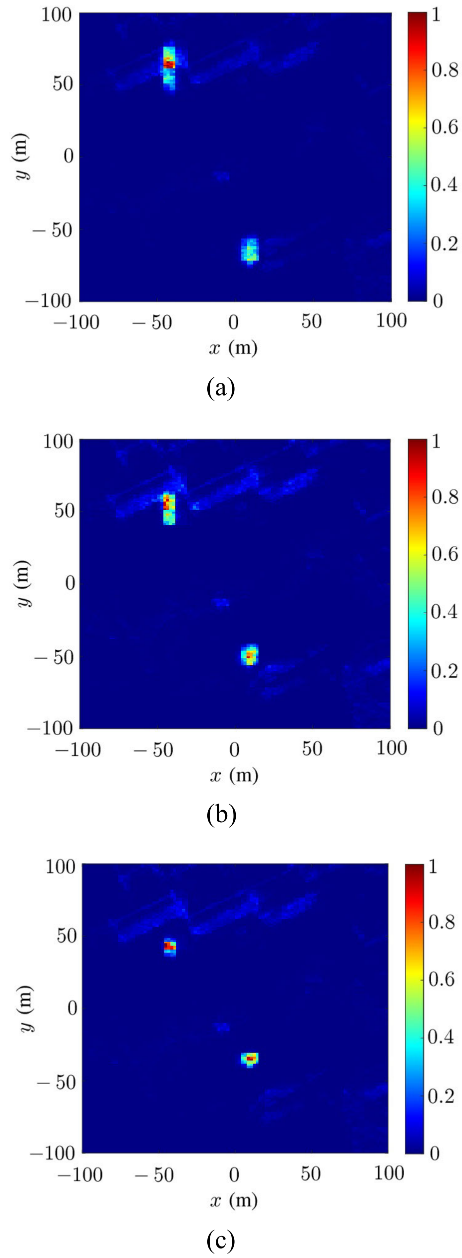

Fig. 12. Enhanced entropy distribution (a) $E^{(1)}(x, y)$, (b) $E^{(3)}(x, y)$, and (c) $E^{(5)}(x, y)$.

where $\gamma_{g1}^{(s)}$ and $\gamma_{g2}^{(s)}$ are the coefficients in the range model of the gth moving target as in (2).

B. Estimation of GMT Range Error With RFRT-FrFT

An RFRT-FrFT is applied to estimate $\gamma_{g1}^{(s)}$ and $\gamma_{g2}^{(s)}$ in (13). First remove the cross-coupled terms, $f_\tau \eta$ and $f_\tau \eta^2$ in $S_{3g}^{(s)}(f_\tau, \eta)$, by applying range frequency reversal transform (RFRT) on $S_{3g}^{(s)}(f_\tau, \eta)$ to have

$$S_g^{(s)}(f_\tau, \eta) = S_{3g}^{(s)}(f_\tau, \eta) S_{3g}^{(s)}(-f_\tau, \eta) = \sum_{n=1}^{N_g} \left(A_{gn}^{(s)}\right)^2 \times \left[\mathrm{rect}\left(f_\tau / B_r\right)\right]^2 e^{-j8\pi f_c R_{0n}^{(s)} / c} \times e^{-j8\pi \left(\gamma_{g1}^{(s)} \eta + \gamma_{g2}^{(s)} \eta^2\right) / \lambda_c} \tag{14}$$

which is inverse Fourier transformed in range to have

$$s_g^{(s)}(\tau, \eta) = \mathcal{F}_\tau^{-1}\left\{S_g^{(s)}(f_\tau, \eta)\right\} = \sum_{n=1}^{N_g} \left(A_{gn}^{(s)}\right)^2 \times \mathrm{sinc}(B_r \tau) e^{-j8\pi R_{0n}^{(s)}/\lambda_c} e^{-j8\pi \left(\gamma_{g1}^{(s)} \eta + \gamma_{g2}^{(s)} \eta^2\right) / \lambda_c} \tag{15}$$

where $\lambda_c = c/f_c$ is the wavelength at the carrier frequency.

Next, apply a fractional Fourier transform (FrFT) to $s_g^{(s)}(\tau, \eta)$ to have [4]

$$S_g^{(s)}(\tau, \phi, u) = \int_{-\infty}^{\infty} K_\phi(u, \eta) s_g^{(s)}(\tau, \eta) d\eta \tag{16}$$

with the kernel

$$K_\phi(u,\eta) = \begin{cases} \sqrt{1-j\cot\phi}\, e^{j\pi\left(\eta^2\cot\phi - 2u\eta\csc\phi + u^2\cot\phi\right)} \\ \qquad\qquad \phi \neq n\pi \\ \delta(u-\eta), \quad \phi = 2n\pi \\ \delta(u+\eta), \quad \phi = (2n\pm 1)\pi. \end{cases}$$

Explicitly, (16) is reduced to

$$S_g^{(s)}(\tau,\phi,u) = \sqrt{1-j\cot\phi}\sum_{n=1}^{N_g}\left(A_{gn}\right)^2 e^{-j8\pi R_{0n}^{(s)}/\lambda_c} \times e^{j\pi u^2\cot\phi}\int_{-T_a/2}^{T_a/2} e^{-j2\pi\left(\alpha_{g1}^{(s)}\eta + \alpha_{g2}^{(s)}\eta^2\right)} d\eta \tag{17}$$

where

$$\alpha_{g1}^{(s)} = \frac{4\gamma_{g1}^{(s)}}{\lambda_c} + u\csc\phi \tag{18}$$

$$\alpha_{g2}^{(s)} = \frac{4\gamma_{g2}^{(s)}}{\lambda_c} - 0.5\cot\phi. \tag{19}$$

If $\alpha_{g2} = 0$, (17) becomes

$$S_g^{(s)}(\tau,\phi,u) = \sqrt{1-j\cot\phi}\sum_{n=1}^{N_g}\left(A_{gn}\right)^2 e^{-j8\pi R_{0n}^{(s)}/\lambda_c} \times e^{j\pi u^2\cot\phi} T_a \operatorname{sinc}\left\{T_a\left(u\csc\phi + 4\gamma_{g1}^{(s)}/\lambda_c\right)\right\} \tag{20}$$

where the sinc function indicates a peak value at $(u,\phi) = (u_g,\phi_g)$, leading to

$$\tilde{\gamma}_{g1}^{(s)} = -\frac{u_g\lambda_c\csc\phi_g}{4}. \tag{21}$$

By substituting the condition $\alpha_{g2}^{(s)} = 0$ and $\phi = \phi_g$ into (19), we have

$$\tilde{\gamma}_{g2}^{(s)} = \frac{\lambda_c\cot\phi_g}{8}. \tag{22}$$

Fig. 13 shows the magnitude of $S_g^{(1)}(\tau,\phi,u)$ after the 7th iteration, with $g = 1$ and $g = 2$, respectively. As the blurred areas containing moving targets shrink with iteration, the peak in Fig. 13 becomes more obvious. Table IV(a) lists the estimated coefficients $\tilde{\gamma}_{g1}^{(s)}$ and $\tilde{\gamma}_{g2}^{(s)}$ and their true values. Define a GMT range error index for target g as follows:

$$\xi_\gamma^{(s)} = 100 \times \frac{\left|\tilde{\bar{\gamma}}_g^{(s)} - \bar{\gamma}_g^{(s)}\right|}{\left|\bar{\gamma}_g^{(s)}\right|}\ (\%)$$

where $\bar{\gamma}_g^{(s)} = [\gamma_{g1}^{(s)}, \gamma_{g2}^{(s)}]^t$ and $\tilde{\bar{\gamma}}_g^{(s)} = [\tilde{\gamma}_{g1}^{(s)}, \tilde{\gamma}_{g2}^{(s)}]^t$. Fig. 14 shows that the GMT range error indices decrease steadily with iteration.

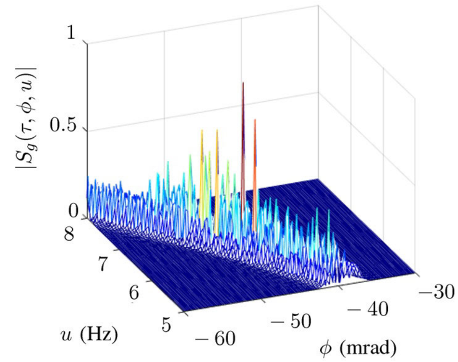

(a)

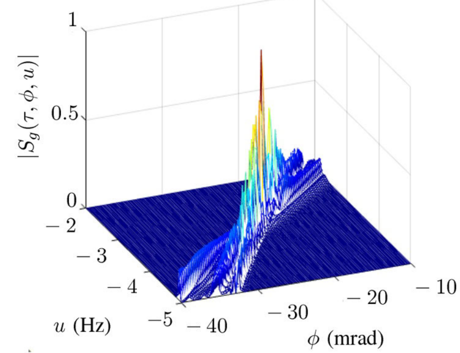

(b)

Fig. 13. Magnitude of $S_g^{(1)}(\tau,\phi,u)$ after 7th iteration (a) $g = 1$ and (b) $g = 2$.

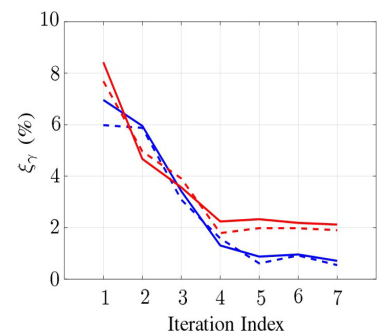

Fig. 14. GMT range error index versus iteration, ——: $g = 1$, $s = 1$, – – –: $g = 1$, $s = 2$, ——: $g = 2$, $s = 1$, – – –: $g = 2$, $s = 2$.

C. Estimation of Target Position and Velocity

The coordinate x_{g0} of the gth moving target is first estimated from the enhanced entropy distribution $E^{(\ell)}(x,y)$ as $\tilde{x}_{g0}$. From (3), v_{gx} is estimated as $\tilde{v}_{gx} \simeq R_0(\tilde{\gamma}_{g1}^{(2)} - \tilde{\gamma}_{g1}^{(1)})/d$, where $R_0^{(1)}$ and $R_0^{(2)}$ are approximated as R_0, which is the range from the reference point Q_0 to the middle point between the two radars at $\eta = 0$.

Next, the velocity component v_{gy} is derived by solving (3) and (4) as follows:

$$\tilde{v}_{gy}^{(s)} \simeq V_p - \frac{1}{|x_0 \mp d/2 + \tilde{x}_{g0}|} \times \left\{\left(\tilde{\gamma}_{g1}^{(s)}\right)^2\left[(x_0 \mp d/2 + \tilde{x}_{g0})^2 - \left(R_0^{(s)}\right)^2\right] + 2R_0^{(s)}\tilde{\gamma}_{g2}^{(s)}(x_0 \mp d/2 + \tilde{x}_{g0})^2\right\}^{1/2}$$

TABLE IV

MOTION PARAMETERS OF MOVING TARGETS. (a) γ COEFFICIENTS. (b) MOVING TARGET 1. (c) MOVING TARGET 2

	γ_{11}	γ_{12}	γ_{21}	γ_{22}
true	1.334	−0.084	−0.858	−0.138
estimated	1.336	−0.087	−0.862	−0.137

(a)

$g=1$	x_{10} (m)	y_{10} (m)	v_{1x}(m/s)	v_{1y}(m/s)	ξ_1(%)
true	10	−20	3	6	-
estimated	10.5	−19.6	2.91	6.27	4.24

(b)

$g=2$	x_{20} (m)	y_{20} (m)	v_{2x}(m/s)	v_{2y}(m/s)	ξ_2(%)
true	−42	32	−2	12	-
estimated	−41.9	31.4	−1.97	12.46	3.79

(c)

where we assume $x_0 \gg |y_{g0}|$ and $V_p \gg |v_{gy}|$. Finally, (3) implies

$$\tilde{y}_{g0}^{(s)} \simeq \frac{\tilde{\gamma}_{g1}^{(1)} R_0^{(s)} - \tilde{v}_{gx}(x_0 \mp d/2 + \tilde{x}_{g0})}{\tilde{v}_{gy} - V_p}$$

and y_{g0} is estimated as $\tilde{y}_{g0} = (\tilde{y}_{g0}^{(1)} + \tilde{y}_{g0}^{(2)})/2$.

Table IV(b) and (c) list the true and estimated position and velocity of the two moving targets. The estimation error on velocity of the gth moving target is defined as follows:

$$\xi_g = 100 \times \frac{|\tilde{\bar{v}}_g - \bar{v}_g|}{|\bar{v}_g|} \ (\%)$$

with $\tilde{\bar{v}}_g = [\tilde{v}_{gx}, \tilde{v}_{gy}]^t$ and $\bar{v}_g = [v_{gx}, v_{gy}]^t$.

Based on the estimated range error of the gth moving target, $\Delta\tilde{R}_g^{(s)}(\eta) = \tilde{\gamma}_{g1}^{(s)}\eta + \tilde{\gamma}_{g2}^{(s)}\eta^2$, a compensation filter is defined as follows:

$$H_{g\gamma}^{(s)}(f_\tau, \eta) = e^{j4\pi(f_c+f_\tau)\Delta\tilde{R}_g^{(s)}(\eta)/c} \times \exp\left\{ j\, 4\pi(f_c+f_\tau)\left(\frac{V_p\tilde{y}_{g0}}{R_0^{(s)}}\eta - \frac{V_p^2}{2R_0^{(s)}}\eta^2\right)\right\} \tag{23}$$

where the first factor compensates for the GMT range error and the second-factor restores $R_{0n}^{(s)}$ in (13) to $R_n^{(s)}(\eta)$ using the relation in (1). By applying the filter in (23) to $S_{3g}(f_\tau, \eta)$ in (13), we obtain an equivalent signal from the gth moving target centered at $(\tilde{x}_{g0}, \tilde{y}_{g0})$

$$\tilde{S}_{3g}^{(s)}(f_\tau, \eta) = H_{g\gamma}(f_\tau, \eta) S_{3g}^{(s)}(f_\tau, \eta) = \sum_{n=1}^{N_g} A_{gn}^{(s)} \mathrm{rect}\,(f_\tau/B_r)\, e^{-j4\pi(f_c+f_\tau)R_n^{(s)}(\eta)/c}.$$

D. Imaging of Individual Moving Target

Take the azimuth Fourier transform of $\tilde{S}_{3g}^{(s)}(f_\tau, \eta)$ to have

$$\tilde{S}_{4g}^{(s)}(f_\tau, f_\eta) = \mathcal{F}_\eta\left\{\tilde{S}_{3g}^{(s)}(f_\tau, \eta)\right\} = \sum_{n=1}^{N_g} A_{gn}^{(s)} \mathrm{rect}\,(f_\tau/B_r) \times e^{-j4\pi(f_c+f_\tau)R_{0n}^{(s)}/c} e^{j2\pi(f_c+f_\tau)(y_{g0}+y_{gn})^2/\left(cR_0^{(s)}\right)} \times e^{-j2\pi f_\eta(y_{g0}+y_{gn})/V_p} e^{j\pi f_\eta^2 cR_0^{(s)}/\left[2(f_c+f_\tau)V_p^2\right]}$$

which is applied with a cross-range compression filter to have

$$\tilde{S}_{5g}^{(s)}(f_\tau, f_\eta) = \tilde{S}_{4g}^{(s)}(f_\tau, f_\eta) H_{\mathrm{crc}}(f_\tau, f_\eta) = \sum_{n=1}^{N_g} A_{gn}^{(s)} \mathrm{rect}\,(f_\tau/B_r)\, e^{-j4\pi(f_c+f_\tau)R_{0n}^{(s)}/c} \times e^{j2\pi(f_c+f_\tau)(y_{g0}+y_{gn})^2/\left(cR_0^{(s)}\right)} \times e^{-j2\pi f_\eta(y_{g0}+y_{gn})/V_p}.$$

By taking the inverse Fourier transform of $\tilde{S}_{5g}^{(s)}(f_\tau, f_\eta)$ in range, followed by the inverse Fourier transform in azimuth, we have the image of the gth moving target

$$\tilde{s}_{7g}^{(s\ell)}(\tau, \eta) = \mathcal{F}_\eta^{-1}\left\{\mathcal{F}_\tau^{-1}\left\{\tilde{S}_{5g}^{(s)}(f_\tau, f_\eta)\right\}\right\} = \sum_{n=1}^{N_g} A_{gn} \mathrm{rect}\,(f_\tau/B_r)\, e^{-j4\pi f_c R_{0n}^{(s)}/c} e^{j2\pi f_c (y_{g0}+y_{gn})^2/\left(cR_0^{(s)}\right)} \times B_r \mathrm{sinc}\left\{B_r\left[\tau - 2R_{0n}^{(s)}/c + (y_{g0}+y_{gn})^2/\left(cR_0^{(s)}\right)\right]\right\} \times F_a \mathrm{sinc}\{F_a[\eta - (y_{g0}+y_{gn})/V_p]\}.$$

The image composed of all the G moving targets after the ℓth iteration is acquired as follows:

$$\tilde{s}_{7G}^{(\ell)}(\tau, \eta) = \sum_{g=1}^{G} \tilde{s}_{7g}^{(\ell)}(\tau, \eta).$$

E. Enhancement of Moving Target Image

The acquired image of moving targets can be further enhanced by iteration. Take the amplitude distribution of the moving target images acquired after the ℓth iteration, $A^{(\ell+1)}(\tau, \eta) = |\tilde{s}_{7G}^{(\ell)}(\tau, \eta)|$, then compute level-$K$ entropy distributions, $E_K^{(\ell+1)}(x, y)$, with $K = 8$, 16, 32, 64, and 128, followed by an enhanced entropy distribution $E^{(\ell+1)}(x, y)$ as in (12). By applying an IRDA process to the two blurred areas, which are smaller than their counterparts in the previous iteration, the moving-target signals are restored as follows:

$$s_{1G}^{(\ell+1)}(\tau, \eta) = \sum_{g=1}^{G} s_{1g}^{(\ell+1)}(\tau, \eta)$$

where $s_{1g}^{(\ell+1)}(\tau, \eta)$ is the restored backscattered signal of the gth moving target in the current iteration. Then, the background signals are separated from the original backscattered signals as follows:

$$s_{1b}(\tau, \eta) = s_1(\tau, \eta) - \sum_{g=1}^{G} s_{1g}^{(\ell+1)}(\tau, \eta).$$

Thus, both the background signals and the moving-target signals are more distinctly separated to acquire better-focused images of $\tilde{s}_{7G}^{(\ell+1)}(\tau, \eta)$ and $\tilde{s}_{7b}(\tau, \eta)$, respectively.

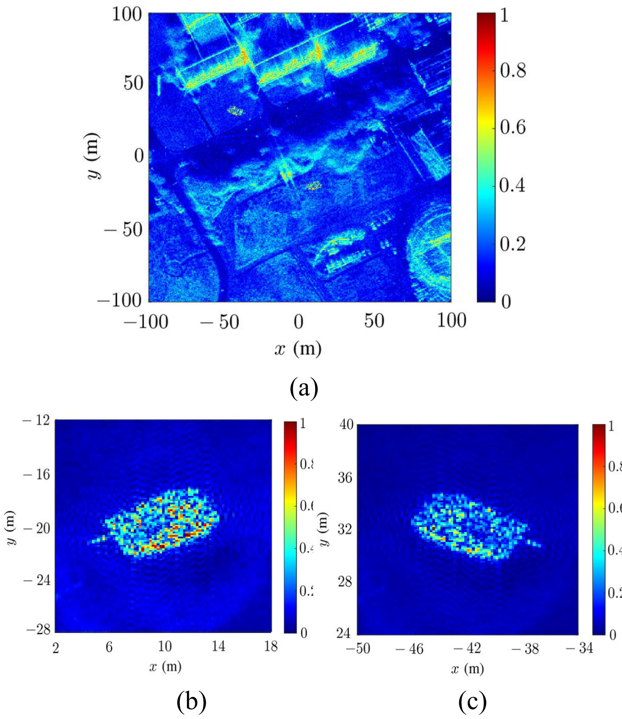

Fig. 15. (a) Acquired SAR image, (b) moving target image, $g = 1$, and (c) moving target image, $g = 2$.

The GMT range error is compensated iteratively until the following criterion is satisfied [28]:

$$\xi^{(\ell)} = \frac{1}{T_a}\int_{-T_a/2}^{T_a/2}\left|\Delta\tilde{R}_g^{(s,\ell)}(\eta) - \Delta\tilde{R}_g^{(s,\ell-1)}(\eta)\right| d\eta < \xi_{\min}$$

where $\Delta\tilde{R}_g^{(s,\ell)}(\eta)$ is the estimated GMT range error in the ℓth iteration, and $\xi_{\min}$ is a tolerance.

Fig. 15(a) shows the final SAR image of the ROI, in which both the background and two moving targets are well focused. Fig. 15(b) and (c) show the magnified images of the two moving targets, respectively.

F. Computational Load and Velocity Error

Table V lists the numbers of multiplications required in various processes of the proposed approach in one iteration. The signal $S_g^{(s)}(f_\tau, \eta)$ after the RFRT process clusters in a narrow strip around the η axis, hence only N_r' ($N_r' \ll N_r$) range-frequency bins are needed for the subsequent FrFT. The grid numbers over ϕ and u in the FrFT process are N_ϕ and N_u, respectively, which determine the resolution of the estimated parameters. The simulations are run with MATLAB R2019a on a PC with i7-3.00 GHz CPU and 32 GB memory.

V. Target Recognition and Highlights

In this section, the acquired images of moving targets are used for recognition to validate their fidelity for field applications. Fig. 16 shows the SAR images and scan images of four different main battle tanks, M1A2 Abrams, Leopard 2, T14 Armata, and ZTZ 99.

Define the intensity (in dB) of an image pixel as follows:

$$I(x, y) = 20\log_{10}|\tilde{s}_{7g}(x, y)|.$$

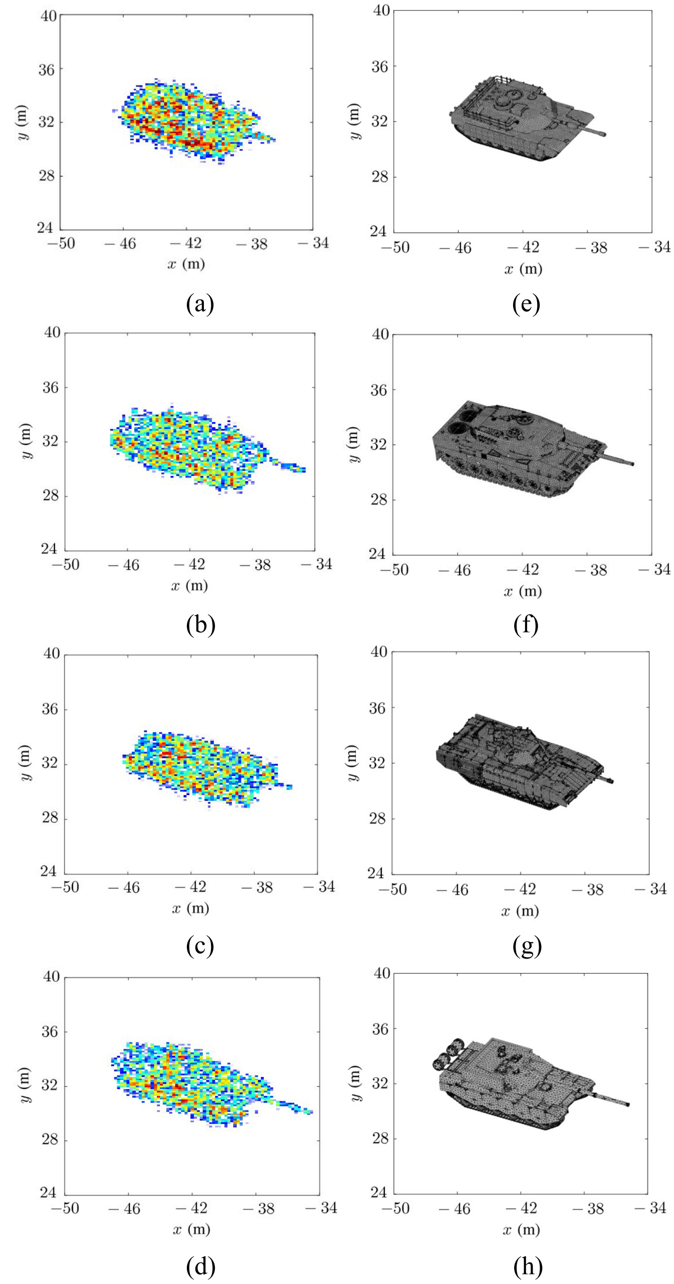

Fig. 16. Images of moving targets (a)–(d) intensity of SAR image and (e)–(h) scan image of 3-D model. (a): M1A2 Abrams, (b): Leopard 2, (c): T14 Armata, and (d): ZTZ 99.

Fig. 17 shows that the cumulative distribution functions (CDFs) of pixel intensity on four different tanks are very similar.

The contour of each target can be delineated by using an edge-enhanced intensity image given by the following equation [47]:

$$I_{vh}(x, y) = \sqrt{I_h^2(x, y) + I_v^2(x, y)}$$

where $I_h(x, y) = I(x, y + \Delta y) - I(x, y - \Delta y)$ enhances horizontal edges and $I_v(x, y) = I(x + \Delta x, y) - I(x - \Delta x, y)$ enhances vertical edges. The edge-enhanced intensity image is then used to determine the center of the target.

TABLE V
COMPUTATIONAL LOAD

process	number of multiplications	ref.
range FFT	$\mathcal{O}(2N_aN_r\log_2 N_r)$	[46]
azimuth FFT	$\mathcal{O}(2N_rN_a\log_2 N_a)$	[46]
range IFFT	$\mathcal{O}(2N_aN_r\log_2 N_r)$	[46]
azimuth IFFT	$\mathcal{O}(2N_rN_a\log_2 N_a)$	[46]
CS-based estimation	$\mathcal{O}(N_a^3)$	
FrFT-based estimation	$\mathcal{O}(N_r'N_\phi N_uN_a)$	
PTD autofocusing	$2\mathcal{O}(2N_aN_r\log_2 N_r)$ $+2\mathcal{O}(2N_aN_r\log_2 N_r)$ $+\mathcal{O}(N_a^3)$	
GMT autofocusing	$2\mathcal{O}(2N_aN_r\log_2 N_r)$ $+3\mathcal{O}(2N_aN_r\log_2 N_r)$ $+\mathcal{O}(N_r'N_\phi N_uN_a)$	
proposed approach	$8\mathcal{O}(2N_aN_r\log_2 N_r)$ $+9\mathcal{O}(2N_aN_r\log_2 N_r)$ $+\mathcal{O}(N_r'N_\phi N_uN_a)$ $+\mathcal{O}(N_a^3)$	

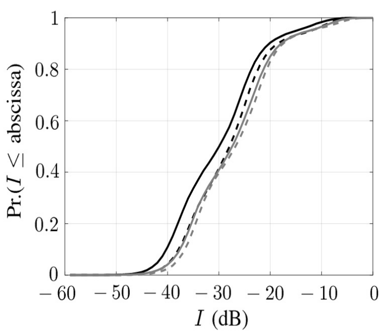

Fig. 17. CDF of pixel intensity in acquired SAR image, ———: M1A2 Abrams, – – –: Leopard 2, ———: T14 Armata, – – –: ZTZ 99.

TABLE VI
INDEX OF CONTOUR MATCHING

ζ_{gq}	M1A2 Abrams	Leopard 2	T14 Armata	ZTZ 99
M1A2 Abrams	0 m	11.83 m	9.86 m	6.72 m
Leopard 2	11.83 m	0 m	7.78 m	11.38 m
T14 Armata	9.86 m	7.78 m	0 m	8.69 m
ZTZ 99	6.72 m	11.38 m	8.69 m	0 m

Next, define an index of contour matching between two edge-enhanced intensity images g and q as follows:

$$\zeta_{gq} = \sqrt{\frac{1}{N_\phi}\sum_{n=0}^{N_\phi-1}|r_g(n\Delta\phi) - r_q(n\Delta\phi)|^2}$$

where N_ϕ is the number of spokes spanned from the target center, at a uniform angular interval of $\Delta\phi = 2\pi/N_\phi$, and $r_g(\phi)$ is the spoke length at angle ϕ in image g. Table VI indicates that ζ_{gq} is an effective index for classifying these four tanks.

A. Real-Data for PTD Compensation

The efficacy of the proposed approach is further verified on a set of real airborne X-band GMT-SAR data in [48], with relevant parameters listed in Table VII. The signals backscattered from a region of 80 × 320 m is processed. Fig. 18(a) shows the acquired SAR image without any compensation, which looks blurred.

TABLE VII
DEFAULT PARAMETERS USED IN [48]

parameter	symbol	value
carrier frequency	f_c	9.6 GHz
range bandwidth	B_r	640 MHz
range sampling rate	F_r	10.72 MHz
pulse duration	T_r	30 μs
range chirp rate	K_r	21.3 THz/s
pulse repetition frequency	F_a	2171.6 Hz
coherent time	T_a	0.858 s
platform velocity	V_p	103.85 m/s
closest slant range	R_0	10.236 km

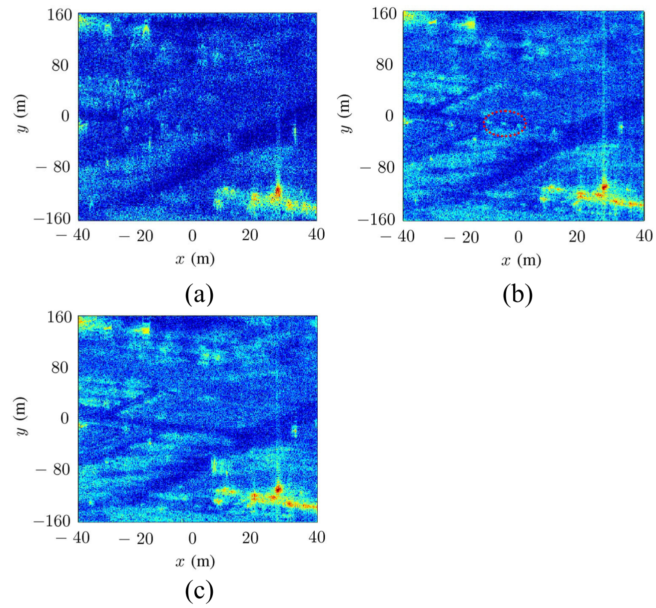

Fig. 18. SAR image acquired from real data [48] (a) without PTD compensation, (b) with PTD compensation, and (c) reference SAR image in [48].

Fig. 18(b) shows the acquired image with platform perturbation compensated with the proposed approach. The image is better focused compared with that in Fig. 18(a). Since a single-channel configuration was adopted in [48], the true target position cannot be accurately estimated.

B. Highlights of Contributions

The contributions of this work are summarized as follows.

1) A dual-channel SAR configuration is proposed to estimate the position of a moving target without azimuth ambiguity.
2) The PTD and GMT phase errors on the background and moving targets are modeled separately and compensated iteratively to acquire focused images.
3) Enhanced entropy distribution is proposed to confine the smeared areas affected by the moving targets.
4) Both images of background and moving targets are enhanced iteratively, preserving most features for recognition.
5) PO theory is used to simulate backscattered signals from moving targets, providing more flexibility to develop SAR imaging methods on targets without measurement data.

VI. Conclusion

A dual-channel SAR imaging approach is proposed to acquire the images of moving targets separately from the stationary background, and the target positions can be accurately estimated. The range error due to platform perturbation and moving targets are represented as polynomials of slow time. The SAR image without compensation is segmented into multiple subimages, on which a CS technique is applied to estimate the polynomial coefficients featuring the platform perturbation. A multilevel enhanced entropy distribution is proposed to confine the image areas affected by the moving targets. An RFRT-FrFT is applied on each confined area to estimate the polynomial coefficients featuring a moving target. The images of both moving targets and the background are further enhanced by iteration. The proposed approach is verified with real and simulated backscattered data, respectively, acquiring images for creditable recognition.

References

[1] J. Pei, Y. Huang, W. Huo, Y. Zhang, J. Yang, and T.-S. Yeo, “SAR automatic target recognition based on multiview deep learning framework,” *IEEE Trans. Geosci. Remote Sens.*, vol. 56, no. 4, pp. 2196–2210, Apr. 2018.

[2] Z. Yang, H. Xu, P. Huang, A. Liu, M. Tian, and G. Liao, “Preliminary results of multichannel SAR-GMTI experiments for airborne quad-pol radar system,” *IEEE Trans. Geosci. Remote Sens.*, vol. 58, no. 6, pp. 3822–3840, Jun. 2020.

[3] M.-S. Kang and K.-T. Kim, “Ground moving target imaging based on compressive sensing framework with single-channel SAR,” *IEEE Sensors J.*, vol. 20, no. 3, pp. 1238–1250, Feb. 2020.

[4] P. Huang, X.-G. Xia, Y. Gao, X. Liu, G. Liao, and X. Jiang, “Ground moving target refocusing in SAR imagery based on RFRT-FrFT,” *IEEE Trans. Geosci. Remote Sens.*, vol. 57, no. 8, pp. 5476–5492, Aug. 2019.

[5] C. Zeng, D. Li, X. Luo, D. Song, H. Liu, and J. Su, “Ground maneuvering targets imaging for synthetic aperture radar based on second-order keystone transform and high-order motion parameter estimation,” *IEEE J. Sel. Topics Appl. Earth Observ. Remote Sens.*, vol. 12, no. 11, pp. 4486–4501, Nov. 2019.

[6] Y. Guo, G. Liao, J. Li, and X. Chen, “A novel moving target detection method based on RPCA for SAR systems,” *IEEE Trans. Geosci. Remote Sens.*, vol. 58, no. 9, pp. 6677–6690, Sep. 2020.

[7] Y. Guo, G. Liao, J. Li, and T. Gu, “A clutter suppression method based on NSS-RPCA in heterogeneous environments for SAR-GMTI,” *IEEE Trans. Geosci. Remote Sens.*, vol. 58, no. 8, pp. 5880–5891, Aug. 2020.

[8] G. Xu, B. Zhang, H. Yu, J. Chen, M. Xing, and W. Hong, “Sparse synthetic aperture radar imaging from compressed sensing and machine learning: Theories, applications, and trends,” *IEEE Geosci. Remote Sens. Mag.*, vol. 10, no. 4, pp. 32–69, Dec. 2022.

[9] G. Xu, B. Zhang, J. Chen, and W. Hong, “Structured low-rank and sparse method for ISAR imaging with 2-D compressive sampling,” *IEEE Trans. Geosci. Remote Sens.*, vol. 60, 2022, Art. no. 5239014.

[10] G. Xu, X.-G. Xia, and W. Hong, “Nonambiguous SAR image formation of maritime targets using weighted sparse approach,” *IEEE Trans. Geosci. Remote Sens.*, vol. 56, no. 3, pp. 1454–1465, Mar. 2018.

[11] G. Jin, Z. Dong, and F. He, “SAR ground moving target imaging based on a new range model using a modified keystone transform,” *IEEE Trans. Geosci. Remote Sens.*, vol. 57, no. 6, pp. 3283–3295, Jun. 2019.

[12] J. Wan, X. Tan, Z. Chen, D. Li, Y. Zhou, and L. Zhang, “Fast approach for SAR imaging of ground moving target with Doppler ambiguity based on 2-D SCFT and IRFCCF,” *IEEE Geosci. Remote Sens. Lett.*, vol. 19, pp. 1–5, 2022.

[13] D. You, G.-C. Sun, M. Xing, Y. Li, and Z. Bao, “SAR ground maneuvering targets imaging and motion parameters estimation based on the adaptive polynomial Fourier transform,” *IEEE Geosci. Remote Sens. Lett.*, vol. 19, pp. 1–5, 2022.

[14] G. Jin, Z. Dong, F. He, and A. Yu, “Background-free ground moving target imaging for multi-PRF airborne SAR,” *IEEE Trans. Geosci. Remote Sens.*, vol. 57, no. 4, pp. 1949–1962, Apr. 2019.

[15] D. Henke, E. M. Dominguez, D. Small, M. E. Schaepman, and E. Meier, “Moving target tracking in SAR data using combined exo- and endo-clutter processing,” *IEEE Trans. Geosci. Remote Sens.*, vol. 56, no. 1, pp. 251–263, Jan. 2018.

[16] Y. Huang, G. Liao, J. Xu, and J. Li, “GMTI and parameter estimation via time-Doppler chirp-varying approach for single-channel airborne SAR system,” *IEEE Trans. Geosci. Remote Sens.*, vol. 55, no. 8, pp. 4367–4383, Aug. 2017.

[17] P. Huang, G. Liao, Z. Yang, X.-G. Xia, J. Ma, and X. Zhang, “An approach for refocusing of ground moving target without target motion parameter estimation,” *IEEE Trans. Geosci. Remote Sens.*, vol. 55, no. 1, pp. 336–350, Jan. 2017.

[18] D. Cristallini and I. Walterscheid, “Joint monostatic and bistatic STAP for improved SAR-GMTI capabilities,” *IEEE Trans. Geosci. Remote Sens.*, vol. 54, no. 3, pp. 1834–1848, Mar. 2016.

[19] D. Cerutti-Maori and I. Sikaneta, “A generalization of DPCA processing for multichannel SAR/GMTI radars,” *IEEE Trans. Geosci. Remote Sens.*, vol. 51, no. 1, pp. 560–572, Jan. 2013.

[20] J. Kim, Y. Kim, T. Yeo, S. Khang, and J. Yu, “Fast Fourier-domain optimization using hybrid L_1/L_p-norm for autofocus in airborne SAR imaging,” *IEEE Trans. Geosci. Remote Sens.*, vol. 57, no. 10, pp. 7934–7954, Oct. 2019.

[21] L. Chen, Z. Liu, and J. Fang, “An accurate motion compensation for SAR imagery based on INS/GPS with dual-filter correction,” *J. Navigat.*, vol. 72, no. 6, pp. 1399–1416, Nov. 2019.

[22] D. E. Wahl, F. H. Eichel, D. C. Ghiglia, and C. V. Jakowatz, “Phase gradient autofocus—A robust tool for high resolution SAR phase correction,” *IEEE Trans. Aerosp. Electron. Syst.*, vol. 30, no. 3, pp. 827–835, Jul. 1994.

[23] Y. Li and S. O’Young, “Kalman filter disciplined phase gradient autofocus for stripmap SAR,” *IEEE Trans. Geosci. Remote Sens.*, vol. 58, no. 9, pp. 6298–6308, Sep. 2020.

[24] J. Li, J. Chen, P. Wang, and O. Loffeld, “A coarse-to-fine autofocus approach for very high-resolution airborne stripmap SAR imagery,” *IEEE Trans. Geosci. Remote Sens.*, vol. 56, no. 7, pp. 3814–3829, Jul. 2018.

[25] G. Wang, M. Zhang, Y. Huang, L. Zhang, and F. Wang, “Robust two-dimensional spatial-variant map-drift algorithm for UAV SAR autofocusing,” *Remote Sens.*, vol. 11, no. 3, p. 340, Feb. 2019.

[26] O. O. Bezvesilniy, I. M. Gorovyi, and D. M. Vavriv, “Autofocusing SAR images via local estimates of flight trajectory,” *Int. J. Microw. Wireless Technol.*, vol. 8, no. 6, pp. 881–889, Sep. 2016.

[27] M.-S. Kang and K.-T. Kim, “Compressive sensing based SAR imaging and autofocus using improved Tikhonov regularization,” *IEEE Sensors J.*, vol. 19, no. 14, pp. 5529–5540, Jul. 2019.

[28] Y.-C. Chen, G. Li, Q. Zhang, Q.-J. Zhang, and X.-G. Xia, “Motion compensation for airborne SAR via parametric sparse representation,” *IEEE Trans. Geosci. Remote Sens.*, vol. 55, no. 1, pp. 551–562, Jan. 2017.

[29] D. Huang, X. Guo, Z. Zhang, W. Yu, and T.-K. Truong, “Full-aperture azimuth spatial-variant autofocus based on contrast maximization for highly squinted synthetic aperture radar,” *IEEE Trans. Geosci. Remote Sens.*, vol. 58, no. 1, pp. 330–347, Jan. 2020.

[30] S. Shi, C. Li, J. Hu, X. Zhang, and G. Fang, “Motion compensation for terahertz synthetic aperture radar based on subaperture decomposition and minimum entropy theorem,” *IEEE Sensors J.*, vol. 20, no. 24, pp. 14940–14949, Dec. 2020.

[31] Z. Liu, S. Yang, Z. Feng, Q. Gao, and M. Wang, “Fast SAR autofocus based on ensemble convolutional extreme learning machine,” *Remote Sens.*, vol. 13, no. 14, p. 2683, Jul. 2021.

[32] J. R. Fienup, “Detecting moving targets in SAR imagery by focusing,” *IEEE Trans. Aerosp. Electron. Syst.*, vol. 37, no. 3, pp. 794–809, Jul. 2001.

[33] L. Ran, Z. Liu, L. Zhang, T. Li, and R. Xie, “An autofocus algorithm for estimating residual trajectory deviations in synthetic aperture radar,” *IEEE Trans. Geosci. Remote Sens.*, vol. 55, no. 6, pp. 3408–3425, Jun. 2017.

[34] L. Ran, Z. Liu, R. Xie, and L. Zhang, “Focusing high-squint synthetic aperture radar data based on factorized back-projection and precise spectrum fusion,” *Remote Sens.*, vol. 11, no. 24, p. 2885, Dec. 2019.

[35] Y. Zhang, J. Sun, P. Lei, G. Li, and W. Hong, “High-resolution SAR-based ground moving target imaging with defocused ROI data,” *IEEE Trans. Geosci. Remote Sens.*, vol. 54, no. 2, pp. 1062–1073, Feb. 2016.

[36] A. R. Brenner, "Ultra-high resolution airborne SAR imaging of vegetation and man-made objects based on 40% relative bandwidth in X-band," in *Proc. IEEE Int. Geosci. Remote Sens. Symp.*, Jul. 2012, pp. 7397–7400.
[37] I. G. Cumming and F. H. Wong, *Digital Processing of Synthetic Aperture Radar Data*. Norwood, MA, USA: Artech House, 2005.
[38] W. G. Carrara, R. S. Goodman, and R. M. Majewski, *Spotlight Synthetic Aperture Radar*. Norwood, MA, USA: Artech House, 1995.
[39] C. V. J. Jakowatz, D. E. Wahl, P. H. Eichel, D. C. Ghiglia, and P. A. Thompson, *Spotlight-Mode Synthetic Aperture Radar: A Signal Processing Approach*. Berlin, Germany: Springer, 2012.
[40] E. D. Jansing, *Introduction to Synthetic Aperture Radar: Concepts and Practice*. New York, NY, USA: McGraw-Hill, 2021.
[41] L. Zhang et al., "Resolution enhancement for inversed synthetic aperture radar imaging under low SNR via improved compressive sensing," *IEEE Trans. Geosci. Remote Sens.*, vol. 48, no. 10, pp. 3824–3838, Oct. 2010.
[42] W. Qiu, H. Zhao, J. Zhou, and Q. Fu, "High-resolution fully polarimetric ISAR imaging based on compressive sensing," *IEEE Trans. Geosci. Remote Sens.*, vol. 52, no. 10, pp. 6119–6131, Oct. 2014.
[43] L. Zhao, L. Wang, G. Bi, and L. Yang, "An autofocus technique for high-resolution inverse synthetic aperture radar imagery," *IEEE Trans. Geosci. Remote Sens.*, vol. 52, no. 10, pp. 6392–6403, Oct. 2014.
[44] *CVX: MATLAB Software for Disciplined Convex Programming*. Accessed: Feb. 15, 2023. [Online]. Available: http://cvxr.com/cvx/
[45] J. Wang, L. Zhang, L. Du, D. Yang, and B. Chen, "Noise-robust motion compensation for aerial maneuvering target ISAR imaging by parametric minimum entropy optimization," *IEEE Trans. Geosci. Remote Sens.*, vol. 57, no. 7, pp. 4202–4217, Jul. 2019.
[46] P. Chen and J. Kiang, "Improved chirp scaling algorithms for SAR imaging under high squint angles," *IET Radar, Sonar Navigat.*, vol. 11, no. 11, pp. 1629–1636, Nov. 2017.
[47] S. Mehrotra, S. Das, S. Shikha, and C. Kar, "Comparative analysis of traditional methods with game of life in cellular automata for edge detection," *Int. J. Comput. Appl.*, vol. 118, no. 17, pp. 18–24, May 2015.
[48] *The Sensor Data Management System, US Air Force*. Accessed: Feb. 15, 2023. [Online]. Available: https://www.sdms.afrl.af.mil/index.php

Dau-Ming Wu was born in Kaohsiung City, Taiwan, September 1995. He received the B.S. degree from the Department of Electronic Engineering, National Changhua University of Education, Changhua, Taiwan, in 2018, and the M.S. degree from the Graduate Institute of Communication Engineering, National Taiwan University, Taipei, Taiwan, in 2022.

He has been working as an Antenna Engineer at Tron Future Tech., Hsinchu City, Taiwan, since August, 2022. His research interests include radar signal processing, synthetic aperture radar (SAR), digital image process, and antenna and electromagnetic circuit design.

Jean-Fu Kiang (Life Senior Member, IEEE) received the Ph.D. degree in electrical engineering from the Massachusetts Institute of Technology, Cambridge, MA, USA, in 1989.

Since 1999, he has been a Professor with the Department of Electrical Engineering, Graduate Institute of Communication Engineering, National Taiwan University, Taipei, Taiwan. His research interest is to explore different ideas, theories, and methods on various electromagnetic phenomena and possible applications, including remote sensing, radar signal processing, antennas, phased arrays, propagation, scattering, communications. Some of his works can be viewed on his website: http://cc.ee.ntu.edu.tw/~jfkiang/selected_publications.html.